International Journal for Housing Science and Its Applications
Publish August 10, 2025. Volume 46, Issue 4 Pages 4817-4826

https://doi.org/10.70517/ijhsa464325

Simulation and analysis of the thermodynamic behavior of high-speed mechanical devices based on the finite difference method

Linli Sun[1,*], Qingsu Liu[1], Haotian Pu[1], Jizheng Pan[1], Zihan Wang[1] and Qiukai Xie[1]
[1] Shaanxi University of Science & Technology, Xi'an, Shaanxi,710068, China
Corresponding authors: (e-mail: 18629197659@163.com).

Abstract High-speed mechanical devices are more and more widely used in modern industry. In view of the thermal accumulation effect of high-speed mechanical devices under extreme working conditions, this paper utilizes the basic principle of spatio-temporal coupled generalized finite difference method to derive the thermal distribution at different locations by Taylor expansion and moving least squares method at separate points. Combined with the Gaussian distribution laser heat source model, the dynamic reconstruction of the thermal field of the device is realized. The study shows that the horizontal error between the solution result of the finite difference method and the actual simulation result is no more than 10 m, and the vertical error is no more than 0.5 m. And the temperature of the X-axis is no more than no more than 1.0 K, and the temperature of the Y-axis has no error. Combined with the solution results for thermal field reduction, the error of thermal field reconstruction is minimized when the reduction angle is set to 145.26°.

Index Terms high-speed mechanical device, heat accumulation, finite difference method, Gaussian distribution, thermal field reconstruction

I. Introduction

With the continuous progress of aerospace and precision manufacturing, its demand for high speed of mechanical devices has become stronger and stronger [1]. And in the high-speed movement, the thermodynamic problem becomes a subject that needs to be emphasized.

First of all, at high speeds, the material is subjected to both radiation and convection heat transfer is very strong, which at different temperatures will lead to different degrees of thermal expansion of the material, resulting in material deformation, reducing the precision of the mechanical device [2], [3]. Secondly, during the high-speed movement of machinery, due to the high pressure on the gas, the gas faces high-speed compression and heating with high energy density, so it is necessary to calculate the parameters of pressure, temperature and density of the gas based on the ideal gas equation of state for thermal analysis [4]-[6]. In addition, at high speeds, the viscous interaction of high-temperature, high-velocity gases with mechanical surfaces leads to an increase in air resistance, which affects the stability of mechanical devices [7], [8]. Finally, when the machinery moves at high speed, the structural components are also subjected to good thermal and pressure loads, triggering irreversible damages such as phase change and creep of the materials, and transient high temperatures are generated in the process of friction of mutual contact of the components, which partially can reach up to 800°C [9]-[11]. Therefore, an adequate thermal analysis of high-speed mechanical devices is required.

The finite difference method is a simpler numerical solution method for solving differential equations on regular grids, and is widely used in the fields of fluid mechanics, structural mechanics, and electric field problems [12]. Compared with the finite element method, the finite difference method is more suitable for high-speed mechanical thermal analysis because it is able to capture microsecond transient thermal shocks and realize parallel computation, which can couple the physical fields such as heat and force, and flexibly deal with different convective boundaries [13]-[15].

This paper analyzes the performance related to the core feed drive system in a high-speed mechanical device. According to the limitations of heat conduction complexity and the high-speed motion objectives of linear motors, the spatio-temporal coupled generalized finite difference method is chosen to solve the thermodynamic behavior. Using the Taylor expansion and the moving least squares method, the functions of each node of the high-speed mechanical device are constructed, and the thermal changes during the operation of the device are obtained by the

nodal solution. Modeling the Gaussian-distributed circular spot laser beam, the temperature distribution of the high-speed mechanical device is restored and its thermal field is reconstructed.

II. Techniques related to thermodynamic analysis of high-speed mechanical devices

II. A.2.1 Analysis of feed drive systems for high-speed mechanical devices

II. A. 1) 2.1.1 Theoretical analysis and calculation of feed drive system selection

To realize very high feed rates of the machining unit while maintaining good acceleration and deceleration characteristics, it is necessary to choose a reasonable feed system. Most of the machines on the market today use a full closed-loop control system, which is realized by means of a multi-head screw with a large lead or a ball screw with a high quality and a small lead. This feed structure has intermediate errors in the transmission, and its own characteristics greatly limit the performance of the feed system. Linear motors convert kinetic energy directly into linear movement, avoiding conversion errors in the intermediate links of transmission components, characterized by fast response, high accuracy, good structural rigidity, large acceleration and deceleration speeds, and low sound in the machining process, but with high manufacturing costs. The application of linear motors in CNC machine tools makes the machine tools have obvious progress in terms of plus and minus characteristics, positioning and repeat positioning accuracy. Also the feed speed aspect is at least 5.0 times higher than conventional motors. The most important feature of this machining device is that all three feeding directions are driven by linear motors, so the calculation and selection of the primary and secondary components of linear motors are particularly important. The X/Y/Z axes are designed for a rapid traverse speed of 125 m/min and a maximum acceleration of 1.5 g. The machining object of the machine is a complex curved surface part, and the surface contour is close to idealized. Based on the above requirements, this machining device is required to have a good axis acceleration at high speed. The selection of linear motors requires good acceleration and deceleration characteristics, which are reflected in shorter acceleration and deceleration times. The selected acceleration time and deceleration time of this machining device is 0.10s, the constant speed time is 0.70s, the dwell time is 0.10s, and the cycle time is 1.0s.

II. A. 2) 2.1.2 Design concepts for feed drive selection

The machining unit in this paper uses two linear motors that straddle each other. Figure 1 shows the linear motor arrangement. Here the X axis bears not only its own mass but also the mass of the Z axis. The Y axis bears not only the mass of the A axis but also the mass of the C axis, i.e. the mass of the CNC rotary table. Considering the difference in the load mass of the three axes, it is set that the load mass of X and Y is 550kg and the load mass of Z is 250kg.

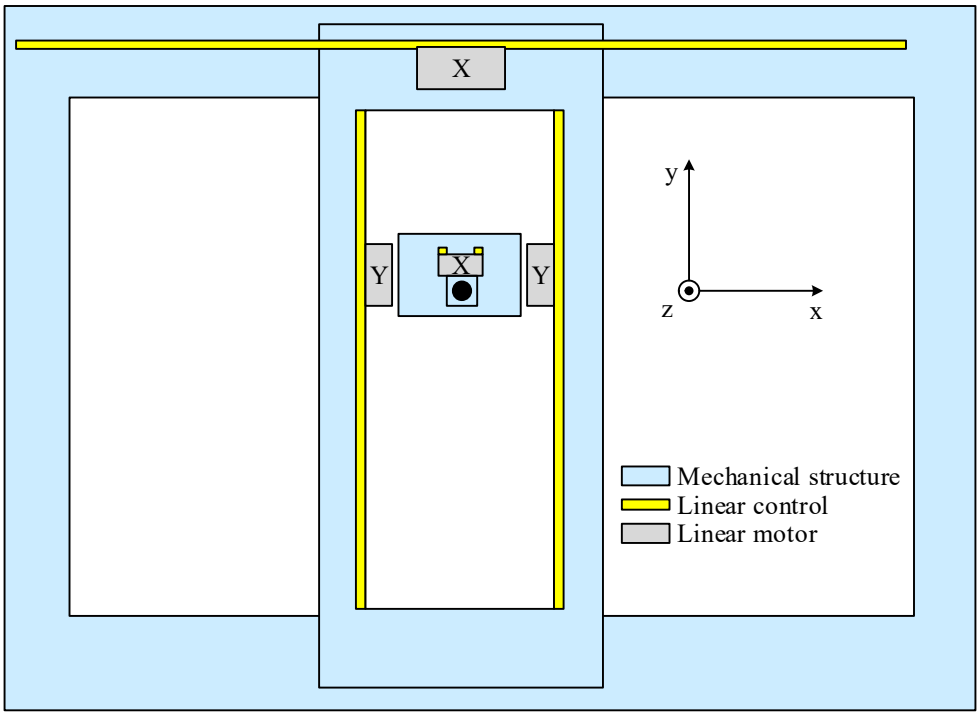

Figure 1: Linear motor axis that crosses the direction of X, Y and Z

The linear motors of the processing device need to have stable motion characteristics, long service life requirements, in addition to the comprehensive consideration from the cost-effective aspect, the linear motors produced by Siemens are selected. First of all, to determine the linear motor selection process, and then according to the selection process to calculate the selection. Figure 2 is the linear motor selection process.

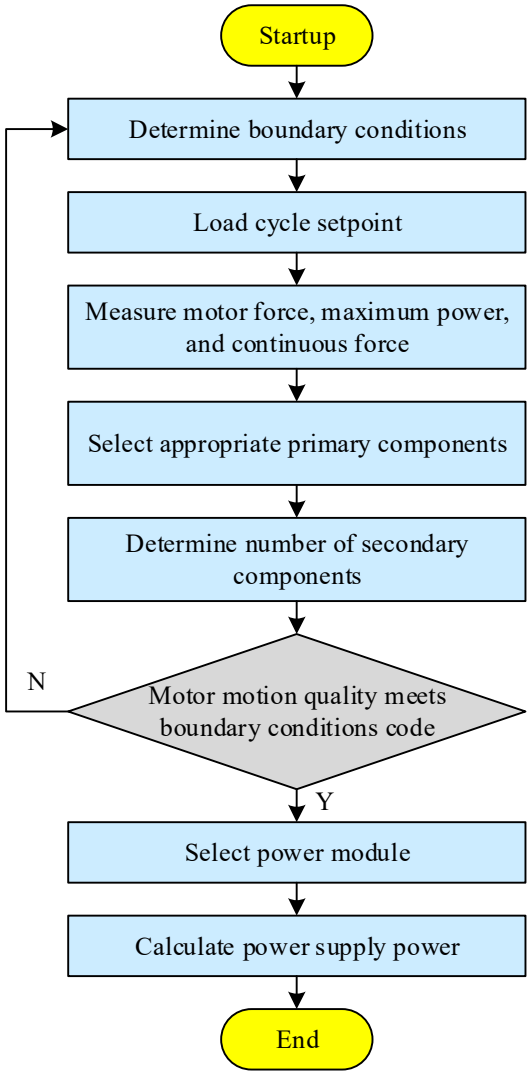

Figure 2: Linear motor selection process

II. B.2.2 Mathematical foundations of the generalized finite difference method for spatio-temporal coupling

The central idea of the generalized finite difference method is to directly introduce the explicit form of the partial derivatives in partial differential equations based on the principle of Taylor expansion with moving least squares. A brief description of how to construct the partial derivatives at each node and the subsequent solution procedure will be presented here.

A set of M nodes are first regularly or randomly scattered in the computational domain Ω^{N+1}. In order not to lose generality, a representative node ξ^I is chosen to demonstrate the solution process. From the nodes around the center node ξ^I, the m nearest nodes $\xi^{I_k}(k=1,2,\ldots,m)$ are selected, and this set of points $E^I=\{\xi^{I_1},\ldots,\xi^{I_m}\}$ is referred to as the center node ξ^I 's “support set”. In this manner, an associated support set is assigned to each node.

Suppose that $U^I \approx U(\xi^I)$ is the function value of the center node ξ^I and $U^k \approx U(\xi^{I_k})$ is the function value of the node $\xi^{I_k}(k=1,2,\ldots,m)$ within the support set E^I. For convenience, the coordinates of node ξ^I in the

extended spatial domain Ω^{N+1} can be expressed as $\xi^I \Omega (x_1^I,\ldots,x_N^I,x_{N+1}^I)$ by introducing $x_{N+1}^I \Omega t^I$. Then, according to the Taylor series expansion, the value of the function $U^k(k=1,2,\ldots,m)$ proximate to the center node ξ^I can be expressed as

$$U^k = U^I + \sum_{i=1}^{N+1} h_i^k \frac{\partial U^I}{\partial x_i} + \frac{1}{2}\sum_{i=1}^{N+1}\sum_{j=1}^{N+1} h_i^k h_j^k \frac{\partial^2 U^I}{\partial x_i \partial x_j} + \ldots, k=1,2,\ldots,m \tag{1}$$

where $h_i^k = x_i^{I_k} - x_i^I$ represents the coordinate step (for $i=1,\ldots,N$) and time interval (for $i=N+1$) from the center point ξ^I to any support point $\xi^{I_k} \in E^I$.

Next, the following residual function $B(U^I)$ can be defined by truncating the Taylor series to the second order

$$B(U^I) = \sum_{k=1}^{m}\left[U^I - U^k + \sum_{i=1}^{N+1} h_i^k \frac{\partial U^I}{\partial x_i} + \frac{1}{2}\sum_{i=1}^{N+1}\sum_{j=1}^{N+1} h_i^k h_j^k \frac{\partial^2 U^I}{\partial x_i \partial x_j}\right]_k^2 \omega_k \tag{2}$$

Here ω_k is a weighting function, and there are many choices for the weighting function, in this paper we use the following form

$$\omega_k = \begin{cases} 1-6\left(\dfrac{d_k}{d_{Max}}\right)^2 + 8\left(\dfrac{d_k}{d_{Max}}\right)^3 - 3\left(\dfrac{d_k}{d_{Max}}\right)^4, & d_k \le d_{Max} \\ 0, & d_k > d_{Max} \end{cases} \tag{3}$$

$$d_k = \left|\xi^{I_k} - \xi^I\right| = \sqrt{\sum_{i=1}^{N+1}(x_i^{I_k} - x_i^I)^2} \tag{4}$$

$$d_{Max} = \max\{d_1, d_2, \ldots, d_m\} \tag{5}$$

where d_k - the generalized distance from the center point ξ^I to the support point ξ^{I_k};

d_{Max} - the maximum generalized distance from the center point ξ^I to the node in the support set.

For the second-order partial differential equation, the following two vectors $D(U^I)$ and p^k are introduced

$$\begin{cases} D(U^I) = \left\{\dfrac{\partial U^I}{\partial x_1},\ldots,\dfrac{\partial U^I}{\partial x_{N+1}},\dfrac{\partial^2 U^I}{\partial x_1^2},\ldots,\dfrac{\partial^2 U^I}{\partial x_{N+1}^2},\dfrac{\partial^2 U^I}{\partial x_1 \partial x_2},\ldots,\dfrac{\partial^2 U^I}{\partial x_i \partial x_j},\ldots,\dfrac{\partial^2 U^I}{\partial x_N \partial x_{N+1}}\right\}^T \\ p^k \Omega p(\xi^{I_k},\xi^I) = \left\{h_1^k,\ldots,h_{N+1}^k,\dfrac{(h_1^k)^2}{2},\ldots,\dfrac{(h_{N+1}^k)^2}{2},h_1^k h_2^k,\ldots,h_i^k h_j^k,\ldots,h_N^k h_{N+1}^k\right\}^T \end{cases} \tag{6}$$

The derivative vector $D(U^I)$ contains all first and second order partial derivatives of the function value U of the center node ξ^I. In order to obtain the desired numerical results, the residual function $B(U^I)$ needs to be minimized. Therefore, differentiating $B(U^I)$ with respect to $D(U^I)$ takes the extrema

$$\frac{\partial B(U^I)}{\partial\{D(U^I)\}} = 0 \tag{7}$$

The following system of linear equations is obtained

$$AD(U^I) = b \tag{8}$$

The coefficient matrix A in Eq. is symmetric and has the following form

$$A = PWP^T \tag{9}$$

$$P = \{p^1, p^2, \ldots, p^m\} \tag{10}$$

$$W = diag(\omega_1^2, \omega_2^2, \ldots, \omega_m^2) \tag{11}$$

The vector b can be expressed as

$$b = PW(U - U^I) \tag{12}$$

$$U = \{U^1, U^2, \ldots, U^m\}^T \tag{13}$$

$$U^I = \{U^I, U^I, \ldots, U^I\}^T \tag{14}$$

The partial derivative vector $D(U^I)$ can then be expressed as

$$\begin{aligned} D(U^I) &= A^{-1}b = A^{-1}PW(U - U^I) \\ &= A^{-1}\left(-\sum_{i=1}^{m}\omega_i^2 p^i\right)U^I + A^{-1}\sum_{i=1}^{m}\omega_i^2 p^i U^i \end{aligned} \tag{15}$$

At this point, the derivative of the unknown function $D(U^I)$ at each node ξ^I in the computational domain can be approximated as a linear combination of the function values at its neighboring nodes (support sets). Expand the above system of equations into the following form

$$D(U^I) = \begin{bmatrix} \dfrac{\partial U^I}{\partial x_1} \\ \vdots \\ \dfrac{\partial U^I}{\partial x_{N+1}} \\ \dfrac{\partial^2 U^I}{\partial x_1^2} \\ \vdots \\ \dfrac{\partial^2 U^I}{\partial x_{N+1}^2} \\ \dfrac{\partial^2 U^I}{\partial x_1 \partial x_2} \\ \vdots \\ \dfrac{\partial^2 U^I}{\partial x_i \partial x_j} \\ \vdots \\ \dfrac{\partial^2 U^I}{\partial x_N \partial x_{N+1}} \end{bmatrix} = \begin{bmatrix} \beta_{x_1}^0 U^I + \sum_{k=1}^{m}\beta_{x_1}^k U^k \\ \vdots \\ \beta_{x_{N+1}}^0 U^I + \sum_{k=1}^{m}\beta_{x_{N+1}}^k U^k \\ \beta_{x_1x_1}^0 U^I + \sum_{k=1}^{m}\beta_{x_1x_1}^k U^k \\ \vdots \\ \beta_{x_{N+1}x_{N+1}}^0 U^I + \sum_{k=1}^{m}\beta_{x_{N+1}x_{N+1}}^k U^k \\ \beta_{x_1x_2}^0 U^I + \sum_{k=1}^{m}\beta_{x_1x_2}^k U^k \\ \vdots \\ \beta_{x_ix_j}^0 U^I + \sum_{k=1}^{m}\beta_{x_ix_j}^k U^k \\ \vdots \\ \beta_{x_Nx_{N+1}}^0 U^I + \sum_{k=1}^{m}\beta_{x_Nx_{N+1}}^k U^k \end{bmatrix} \tag{16}$$

where $\{\beta_{x_1}^k, \ldots, \beta_{x_{N+1}}^k, \beta_{x_1x_1}^k, \ldots, \beta_{x_{N+1}x_{N+1}}^k, \beta_{x_1x_2}^k, \ldots, \beta_{x_ix_j}^k, \ldots, \beta_{x_Nx_{N+1}}^k\}_{k=0}^m$ is the weighting coefficient corresponding to node ξ^I and is obtained through the numerical calculation process described above. Finally, Equation (16) is substituted into the control equations or boundary conditions corresponding to each node to integrate the establishment of a system of linear algebraic equations, which is solved to obtain the function values at each node.

II. C.2.3 Gaussian Distributed Laser Heat Transfer

A Gaussian-distributed circular spot laser beam is modeled and its transverse model is shown in Figure 3.

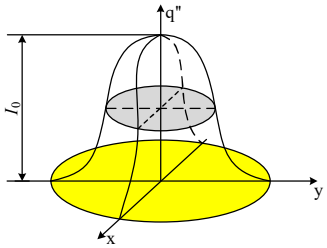

Figure 3: Lateral model of the laser spot

Its Gaussian heat flux distribution takes the following exponential form:

$$q'' = \begin{cases} I_0 \times e^{\frac{-k(x^2+y^2)}{r^2}} & vt-r<x<vt+r \\ & -\sqrt{r^2-(x-vt)^2}<y<\sqrt{r^2-(x-vt)^2} \\ & Or\ z=0 \\ 0 & Other \end{cases} \tag{17}$$

where I_0 denotes the light intensity at the center of the laser spot, k is a constant (usually taking the value 2.0), r is the spot radius, and:

$$r = \sqrt{\frac{s}{\pi}} \tag{18}$$

where s denotes the area of the laser action region, in general the laser power will be given directly, the laser center light intensity I_0 can be obtained by the following expression:

$$\int_{-r}^{r} \int_{-\sqrt{r^2-x^2}}^{\sqrt{r^2-x^2}} I_0 \times e^{\frac{-k\sqrt{x^2+y^2}}{r^2}} dydx = q_0 \tag{19}$$

Substituting equation (17) into equation (16) is obtained by collation:

$$\begin{aligned} &\int_0^a \int_{-b/2}^{b/2} \int_0^h q'''(x,y,z,t) \times X(o,x) \times P(p,y) \times Z(q,z) dxdydz \\ &= \int_{vt-r}^{vt+r} \int_{-\sqrt{r^2-(x-vt)^2}}^{\sqrt{r^2-(x-vt)^2}} I_0 \times e^{\frac{-k(y^2+(x-vt)^2)}{r^2}} \cos(\alpha(o)x)\cos(\beta(p)y) dydx \\ &= \psi(o,p,q,t) \times \frac{abh}{8} \end{aligned} \tag{20}$$

In order to solve $\psi(o,p,q,t)$ The Newton-Cotes formula is introduced here and the central idea is to construct the product formula using Lagrange interpolating polynomials given as follows:

$$p_n(x) = \sum_{k=0}^{n} \prod_{\substack{i=0 \\ i \neq k}}^{n} \frac{x-x_i}{x_k-x_i} f(x_k) \tag{21}$$

The $p_n(x)$ in the above equation is an approximation of $f(x)$, which is obtained by transforming equation (21) using its approximation properties:

$$\begin{cases} I(p_n) = \sum_{k=0}^{n} A_k^n f(x_k) \\ A_k^n = \int_a^b \rho(x) \prod_{\substack{i=0 \\ i \neq k}}^{n} \frac{x-x_i}{x_k-x_i} dx \quad k = 0,1,\ldots n \end{cases} \tag{22}$$

It is clear that the product coefficients of the constructed product formula are related only to the weight function, the integration interval and the interpolating nodes, and not to the product function. When the weight function in Eq. (22) is constant at 1.0 and the nodes are taken to be equidistant nodes, thus forming the Newton-Cotes formula. Then the second equation in Eq. (22) can be rewritten as:

$$A_k^n = \frac{b-a}{n} \int_0^n \prod_{\substack{i=0 \\ i \neq k}}^{n} \frac{t-i}{k-i} dt = (b-a)c_k^n \tag{23}$$

Among them:

$$\begin{cases} c_k^n = \dfrac{1}{n}\int_0^n \prod_{\substack{i=0 \\ i\neq k}}^{n} \dfrac{t-i}{k-i}dt = \dfrac{(-1)^{n-k}}{n(n-k)!k!}\int_0^n \dfrac{\pi_n(t)}{t-k}dt \\ \pi_n(t) = t(t-1)(t-2)\cdots(t-n) \quad k = 0,1,\ldots n \end{cases} \tag{24}$$

For ease of representation, the Cotes coefficient c_k^n is usually expressed as a quotient of two integers, i.e., $c_k^n = a_k^n / b^n (k = 0,1,\ldots n)$.

List the values of a_k^n and b^n corresponding to different values of n.

Solve for the numerical solution of $\psi(o,p,q,t)$ using the above method to obtain the corresponding $\theta(o,p,q,t)$ values for the temperature field $\Delta T(x,y,z,t)$, where:

$$\theta(o,p,q,t) = \int_0^t \Omega(o,p,q,t) \times e^{-\omega(o,p,q)(t-\tau)} d\tau \tag{25}$$

III. Application of the finite difference method to the analysis of the thermodynamic behavior of high-speed mechanical devices

III. A. 3.1 Numerical testing of the finite difference method

III. A. 1) 3.1.1 Analysis of solution accuracy

The high-speed machining device proposed in this paper is selected as the research object. In order to judge whether the finite difference method can accurately solve to obtain the heat conduction at each position of the device and complete the Gaussian distribution laser heat conduction modeling. In this section, numerical tests are set up before the actual analysis practice to verify the solution effect of the finite difference method. The high-speed machining device model is meshed, with the grid spacing taken as 15m, the number of grids in the X-direction is 200, and the number of grids in the Y-direction is 70, and the thickness variation of the thermal value at Y=35 in the middle profile is studied. Figure 4 shows the comparison between the simulation results and the analytical solution results of the finite difference method. The solid line represents the actual simulation results and the dashed line represents the analytical solution results of the finite difference method. The simulation results at t=0s, 15s and 30s are taken to compare with the analytical solution results, respectively. In the model range of large-scale high-speed machining equipment with horizontal distance from -750 m to 750 m and elevation from 0 to 15 m, the error between the simulation results and the analytical solution results of the finite-difference method is no more than 10 m and 0.5 m. The finite-difference method can numerically restore the thermal condition of the high-speed machining equipment, no matter the horizontal distance or the elevation.

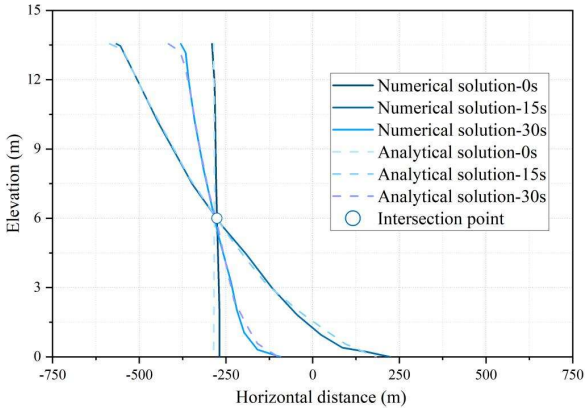

Figure 4: Comparison between simulation results and analytical solution results

III. A. 2) 3.1.2 Thermal field fluctuation curvature analysis

After solving the thermal field of the overall high-speed machining device, since the device is used for the machining of complex curved parts, it is also necessary to analyze the effectiveness of the finite difference method in the fluctuating surface conditions, and to examine the impact of combining the thermal solution under the action of the off/centripetal force. Assuming the simultaneous machining of four surface parts, the high-speed machining device has four rises, with a certain curvature between the rises, and the parts are subjected to centripetal force when moving between the rises. The parts are distributed between the slopes before machining, and the part morphology is symmetrically distributed. Figure 5 shows the results of solving the radius of curvature at the fluctuation of the thermal field. It can be seen from the thermal field reduced by solving that the radius of curvature at 4 places are

4.47m, 14.65m, 15.96m and 10.02m, which are consistent with the radius of curvature in the delineation mesh, and the effect of the thermal field solved and reduced is good.

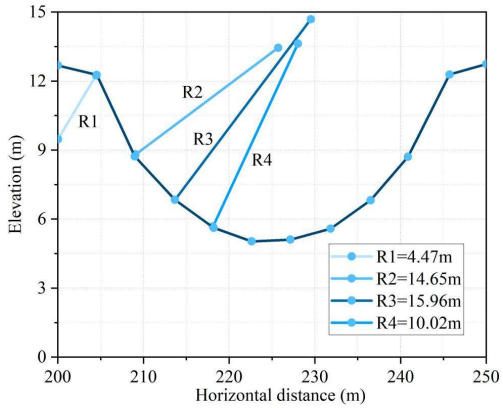

Figure 5: Solution of the radius of curvature at the wave of the thermal field

III. A. 3) 3.1.3 Numerical stability analysis

The thickness and volume distributions of the reduced thermal field are statistically analyzed, and Table 1 shows the volume distribution statistics. Whether considering centrifugal action or no centrifugal action, the volume and proportion of the thermal field of the four surfaces are in the order of size: surface 3>surface 2>surface 4>surface 1, and the maximum thickness of the four surfaces also has the same ordering results, which is consistent with the results of the radius of curvature analysis. Therefore, it can be judged that the distribution of the thermal field of the high-speed mechanical device obtained by combining the finite difference method of solving the reduction is consistent with the actual device heat generation, and it is feasible to use the finite difference method of solving the thermal value of the device at various places.

Table 1: Volume distribution statistics

Distribution position	Volume /m ³ (centrifugal)	Proportion /% (Centrifugation)	Maximum thickness /m (centrifugal)	Volume /m ³ (without centrifugation)	Proportion /% (without centrifugation)	Maximum thickness /m (without centrifugation)
Surface 1	5028.1	13.7	3.5	4897.5	14.2	2.6
Surface 2	10423.5	28.3	10.3	10021.3	29.0	8.9
Surface 3	12365.8	33.6	11.2	11004.6	31.8	10.4
Surface 4	8957.6	24.4	6.6	8610.4	24.9	5.8

III. B. 3.2 Practice of Finite Difference Method (FDM)-based analysis of thermodynamic behavior

III. B. 1) 3.2.1 Thermodynamic behavior of high-speed mechanical devices in the axial direction

The finite difference method after verification of validity is utilized to calculate the thermodynamic conditions of the X-axis and Y-axis of the high-speed mechanical device undergoing machining operations and to compare them with the actual thermodynamic conditions. Figure 6 shows the thermodynamic behavior of the high-speed mechanical device in the axis direction. The dots represent the temperature distribution of each component, and the lines show the actual temperature situation. When the high-speed mechanical device is working, the temperature of each component position in the X-axis and Y-axis directions varies between 0-250 K. The temperature distribution in the X-axis ranges from 6.08 m to 13.71 m, while that in the Y-axis ranges from 6.83 m to 13.91 m. The temperature distribution in the X-axis is wider. Comparing the solution calculated by the finite difference method with the actual temperature distribution, the temperature difference is not more than 1.00K, and the temperature difference mainly occurs in the X-axis direction in the more extreme temperature positions (0-50K, 200-250K), the temperature calculation difference in the rest of the positions is small, and there is even no calculation error in the Y-axis direction.

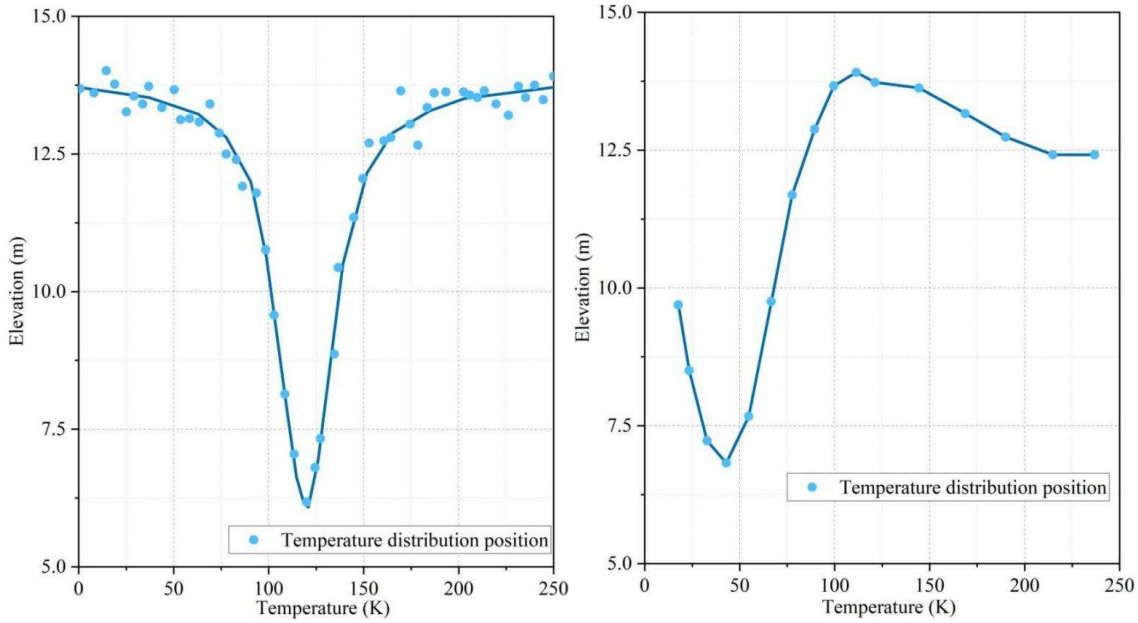

(a) X (b) Y

Figure 6: The axial thermodynamic behavior of high-speed mechanical devices

III. B. 2) 3.2.2 Error analysis of thermal field reconstruction for high-speed mechanical devices

According to the thermal distribution in all directions obtained from the solution, the thermal field reduction of the high-speed mechanical device is carried out at different angles (θ), and its error is also compared to determine the most suitable reduction angle. Figure 7 shows the thermal field reconstruction and its error based on the results of the finite difference method. 0.47m at 145.26° and 0.62m at 15.44° are the smallest errors in the thermal field reduction at different angles from 0 to 180°, and the largest error is 0.62m at 15.44°. Therefore, after solving for the thermal distribution of the high-speed mechanical device, the smallest thermal field reduction error is obtained by taking 145.26° as the reduction angle, and the largest thermal field reduction error is obtained by taking 145.26° as the reduction angle. Field reduction error, maximize the understanding of the thermodynamic behavior of high-speed mechanical devices in the working process, and provide reference for managers to carry out mechanical device maintenance.

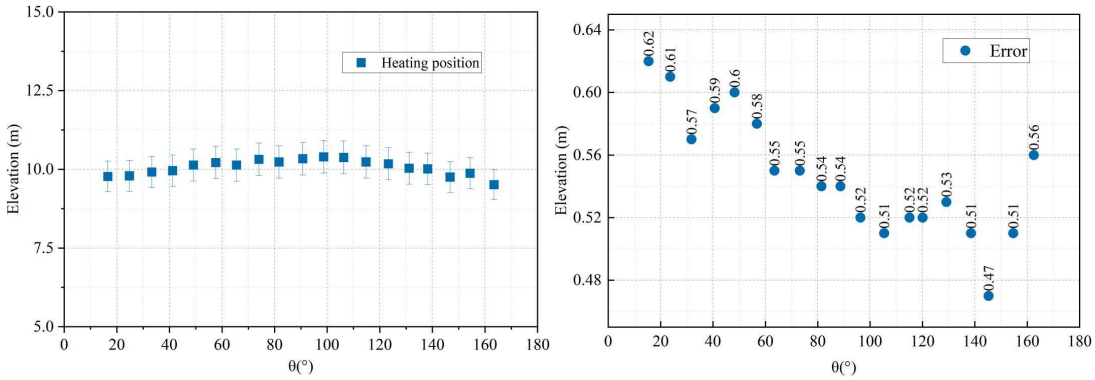

(a) Thermal field reconstruction from different perspectives (b) Reconstruction error

Figure 7: Thermal field reconstruction and its errors

IV. Conclusion

In this paper, the spatio-temporally coupled generalized finite difference method is used to resolve the thermodynamic behavior of a linear motor-driven high-speed mechanical device. The error of this method is less than 10 m in the horizontal solution of the device, and less than 0.5 m in the vertical solution. The radii of curvature

of the thermodynamic field restored by the solution are 4.47 m, 14.65 m, 15.96 m, and 10.02 m respectively, which are in line with the actual ones. The error of the solution for the temperature positions of 0-50K and 200-250K in the direction of the X-axis is not more than 1.00 K, and the errors for the rest of the positions are smaller or no error. or no error. The errors of the reconstructed thermal field at different angles range from 0.47m to 0.62m, and the error is the smallest when the reduction angle is 145.26°. In the future, we can focus on optimizing the stability of the numerical solution of the finite difference method to improve the accuracy of thermodynamic behavior analysis.

References

[1] Chao, Q., Zhang, J., Xu, B., Huang, H., & Pan, M. (2019). A review of high-speed electro-hydrostatic actuator pumps in aerospace applications: challenges and solutions. Journal of Mechanical Design, 141(5), 050801.

[2] Gu, Y., Wang, X., Gao, P., & Li, X. (2021). Mechanical analysis with thermal effects for high-speed permanent-magnet synchronous machines. IEEE Transactions on Industry Applications, 57(5), 4646-4656.

[3] Liang, X., Liu, Z., Wang, B., & Hou, X. (2018). Modeling of plastic deformation induced by thermo-mechanical stresses considering tool flank wear in high-speed machining Ti-6Al-4V. International Journal of Mechanical Sciences, 140, 1-12.

[4] Olmedo, L. E., Liu, W., Gjika, K., & Schiffmann, J. (2023). Thermal management for gas lubricated, high-speed turbomachinery. Applied Thermal Engineering, 218, 119229.

[5] Houidi, M. B., Sotton, J., Bellenoue, M., & Strozzi, C. (2019). Effects of low temperature heat release on the aerodynamics of a flat piston rapid compression machine: Impact on velocity and temperature fields. Proceedings of the combustion institute, 37(4), 4777-4785.

[6] Yu, M., Peng, X., Meng, X., Jiang, J., & Ma, Y. (2023). Influence of cavitation on the heat transfer of high-Speed mechanical seal with textured side wall. Lubricants, 11(9), 378.

[7] Song, L., Yu, J., Yu, Y., Wang, Z., Wu, S., & Gao, R. (2023). An experimental study on the resistance of a High-Speed air cavity craft. Journal of Marine Science and Engineering, 11(7), 1256.

[8] Gao, F., Jia, W., Li, Y., Zhang, D., & Wang, Z. (2021). Analysis and experimental research on the fluid–solid coupled heat transfer of high-speed motorized spindle bearing under oil–air lubrication. Journal of Tribology, 143(7), 071801.

[9] Luo, F., Ma, C., Liu, J., Yang, L., & Zhou, W. (2023). Effect of gas–liquid phase change of axial rotating heat pipe on fluid-thermal-solid behaviors of high-speed spindle. Applied Thermal Engineering, 232, 121117.

[10] Liu, Y., Wang, B., Yang, S., Liao, Y., & Guo, T. (2022). Characteristic analysis of mechanical thermal coupling model for bearing rotor system of high-speed train. Applied Mathematics and Mechanics, 43(9), 1381-1398.

[11] Dong, Y., Ma, Y., Qiu, M., Chen, F., & He, K. (2024). Analysis and experimental research of transient temperature rise characteristics of high-speed cylindrical roller bearing. Scientific Reports, 14(1), 711.

[12] Stynes, M., O'Riordan, E., & Gracia, J. L. (2017). Error analysis of a finite difference method on graded meshes for a time-fractional diffusion equation. SIAM Journal on Numerical Analysis, 55(2), 1057-1079.

[13] Qin, J., Chen, Y., Lin, Y., & Deng, X. (2023). On construction of shock-capturing boundary closures for high-order finite difference method. Computers & Fluids, 255, 105818.

[14] Rostami, S. R. M., & Ghaffari-Miab, M. (2019). Finite difference generated transient potentials of open-layered media by parallel computing using openmp, mpi, openacc, and cuda. IEEE Transactions on Antennas and Propagation, 67(10), 6541-6550.

[15] Meyghani, B., Awang, M. B., Emamian, S. S., Mohd Nor, M. K. B., & Pedapati, S. R. (2017). A comparison of different finite element methods in the thermal analysis of friction stir welding (FSW). Metals, 7(10), 450.